Detecting Reactivation Mechanisms of an Active Landslide Using LiDAR-Derived Stem-Lean Metrics and Electrical Resistivity Tomography

Julias, H. R.,[1, 4] Sartohadi, J.[2,4*] and Samodra, G.[3]
[1]Geo-Information for Disaster Management and Spatial Planning, Graduate School, Universitas Gadjah Mada, Indonesia
E-mail: husna.rafi25@gmail.com, ORCID ID: https://orcid.org/0009-0002-1798-1143
[2]Department of Soil Science, Universitas Gadjah Mada, Indonesia
E-mail: junun@ugm.ac.id,* ORCID ID: https://orcid.org/0000-0002-0059-8335*
[3]Department of Environmental Geography, Universitas Gadjah Mada, Indonesia
E-mail: guruh.samodra@ugm.ac.id, ORCID ID: https://orcid.org/0000-0002-4094-8846
[4] Research Center for Land Resources Management, Universitas Gadjah Mada, Indonesia
Corresponding Author

DOI: https://doi.org/10.52939/ijg.v22i7.5079

Abstract
Identification of reactivation zones in thick volcanic soils is critical for understanding landslide mechanisms. Volcanic soils are clay-rich, making slopes highly susceptible to water saturation and renewed movement. However, scientific understanding of the relationship between surface indicators and subsurface structure remains limited, particularly in thick and well-developed volcanic terrains. Few studies have combined vegetation-based deformation with subsurface resistivity structure within a single framework. This study integrates unmanned aerial vehicle (UAV)-based LiDAR and electrical resistivity tomography (ERT) to characterize an active landslide in Kalisari, Central Java, Indonesia. ERT serves as a non-invasive method to map subsurface moisture and weak zones. UAV-LiDAR data were processed to generate a detailed terrain representation of the landslide. The UAV-LiDAR point cloud was used to extract surface morphology and vegetation-based deformation metrics, including tree stem-lean angle and azimuth. ERT surveys were conducted along multiple profiles across the landslide to delineate low-resistivity zones interpreted as saturated clay-rich materials. Results indicate that reactivation areas are clearly expressed by surface morphology and coherent stem-lean patterns. Although the overall morphology is rotational, recent movement is dominated by coherent lateral displacement. Stem-lean orientations align with the inferred movement direction (azimuth 45–100°). LiDAR-derived stem-lean estimates show good agreement with field measurements ($R^2 = 0.87$ for lean angle and $\rho^2 = 0.85$ for azimuth). ERT results also show that reactivation areas correspond to low-resistivity zones (3–30 $\Omega \cdot m$) that spatially coincide with surface cracks, flow-accumulation features, and stem-lean anomalies. This indicates that water infiltration through surface discontinuities recharges the weak saturated clay layer and makes the slope more prone to instability. Overall, integrating UAV-LiDAR and ERT provides a strong basis for linking surface deformation with subsurface structure and identifying landslide reactivation zones in volcanic landscapes.

Keywords: ERT, Landslide Reactivation, Morphology, Stem Lean, UAV-LiDAR

1. Introduction

Landslides on thick volcanic soils are among the most destructive geomorphic processes in tropical mountain regions. Their impacts are far-reaching, including damage to settlements and infrastructure, disruption of river systems, and an increase in long-term sediment supply [1] and [2]. In volcanic areas, these landslides are favored where intense weathering of pyroclastic deposits and andesitic breccias produce a very thick regolith [3] and [4]. This regolith has a high clay content, becomes easily saturated, and is mechanically weak [5]. Deep-seated landslides frequently undergo phases of reactivation and do not terminate in a single event. They may evolve through headward retreat, block translation, and bulging at the slope toe [6] and [7]. Therefore, the identification of landslide reactivation zones is

ISSN: 1686-6576 (Printed) | ISSN 2673-0014 (Online) |

critical for mitigation planning [8]. Landslide reactivation refers to the renewed movement of a previously failed slope mass, often characterized by distinct patterns of movement that differ from the initial failure phase [9].

High-resolution remote sensing offers new opportunities to characterize landslide reactivation. Light detection and ranging (LiDAR) data acquired from unmanned aerial vehicles (UAVs) can now provide very high-resolution topographic information [10] and [11]. Numerous studies have used LiDAR to map landslide morphology in detail, derive morphometric parameters, and monitor surface deformation [12] and [13]. Surface deformation on densely vegetated slopes is difficult to detect because tree canopies often obscure the ground surface. As a result, vegetation-based approaches have emerged as additional indicators for detecting slope movement [8]. Dendrogeomorphological studies show that the magnitude and direction of stem lean record information about slope movement mechanisms and can even help distinguish between landslide types [14][15] and [16].

Field measurements of stem lean still face several challenges. Their spatial coverage is limited, and it is difficult to represent deformation patterns over the entire landslide body. Terrestrial LiDAR has recently been used to systematically map leaning stems [17]. However, the full potential of extracting vegetation metrics from UAV-LiDAR point clouds for landslide diagnostics has not yet been explored in depth [18]. Another approach to diagnose landslide reactivation zones is the geophysical method of electrical resistivity tomography (ERT). Numerous studies have shown that ERT is effective in estimating the position of the slip surface, delineating water-saturated clay layers, and assessing the role of hydrological conditions in slope instability [19][20] and [21]. However, the spatial relationships between resistivity anomalies, surface morphology, and stem-lean patterns have not been widely explored [22]. Addressing this gap requires an approach that captures surface deformation and subsurface structure together. The Kalisari landslide in Central Java is a representative case. It lies in the Sumbing volcanic region, where recurrent landslides on thick clay-rich soils threaten settlements and farmland [3]. Dense vegetation and deep regolith there limit direct observation of surface and subsurface conditions [23]. UAV-LiDAR addresses the surface limitation and ERT the subsurface limitation. Applying both methods together is therefore well suited to characterizing reactivation at this site.

This study integrates UAV-LiDAR and ERT to characterize reactivation zones in an active landslide. Two hypotheses are tested in this study. First, detailed morphology and stem-lean metrics derived from LiDAR can serve as indicators of slope deformation. Second, the integration of surface and subsurface information can delineate the parts of the landslide body that are most susceptible to reactivation. The objectives of this study are to develop and validate LiDAR-based stem-lean extraction, to map saturated zones and weak layers using ERT, and to combine both datasets to diagnose the spatial structure and hydromechanical controls of reactivation.

2. Materials and Methods

2.1 Study Area and Instruments

The study was conducted at the active Kalisari landslide in Magelang Regency, Central Java, Indonesia (7°33′48.32″ S, 110°03′57.37″ E) from 1 February 2024 to 31 August 2024 (Figure 1(a) and 1(d)). The survey period was selected to span the transition from the wet to dry season. This timing allowed capture of fresh deformation signals from the preceding rainy season, since slope movement is typically most pronounced shortly after periods of intense rainfall. The ERT survey was carried out under drier conditions, as excessive soil moisture can compromise electrode contact and reduce the reliability of resistivity measurements. The site lies within the Bompon sub-watershed (Figure 1(c)), a transition zone between the Quaternary Sumbing volcano and the Neogene Menoreh Mountains [24], see (Figure 1(b)). The area is underlain by thick volcanic soils overlying altered andesitic breccia bedrock that is mechanically weak and easily saturated [23]. Land use is dominated by mixed gardens on steep slopes. This setting provides a sufficient number of leaning trees to test stem lean as an indicator of slope deformation. Aerial imagery was acquired using a DJI Mavic 3 Enterprise and processed photogrammetrically to produce a high-resolution orthophoto. LiDAR point clouds were collected using a DJI Matrice 300 equipped with a Zenmuse L1 sensor. Subsurface resistivity was measured using an OYO McOHM ERT system with stainless-steel electrodes. The ERT system injects a low-frequency square-wave current. This minimizes electrode polarization and self-potential effects and provides a stable measurement of resistivity.

The current frequency is fixed by the instrument and was not varied during the survey. A geodetic Global Navigation Satellite System (GNSS) receiver (Emlid Reach RS2) was used to measure ground control points (GCPs) and to record precise elevations at each ERT electrode location.

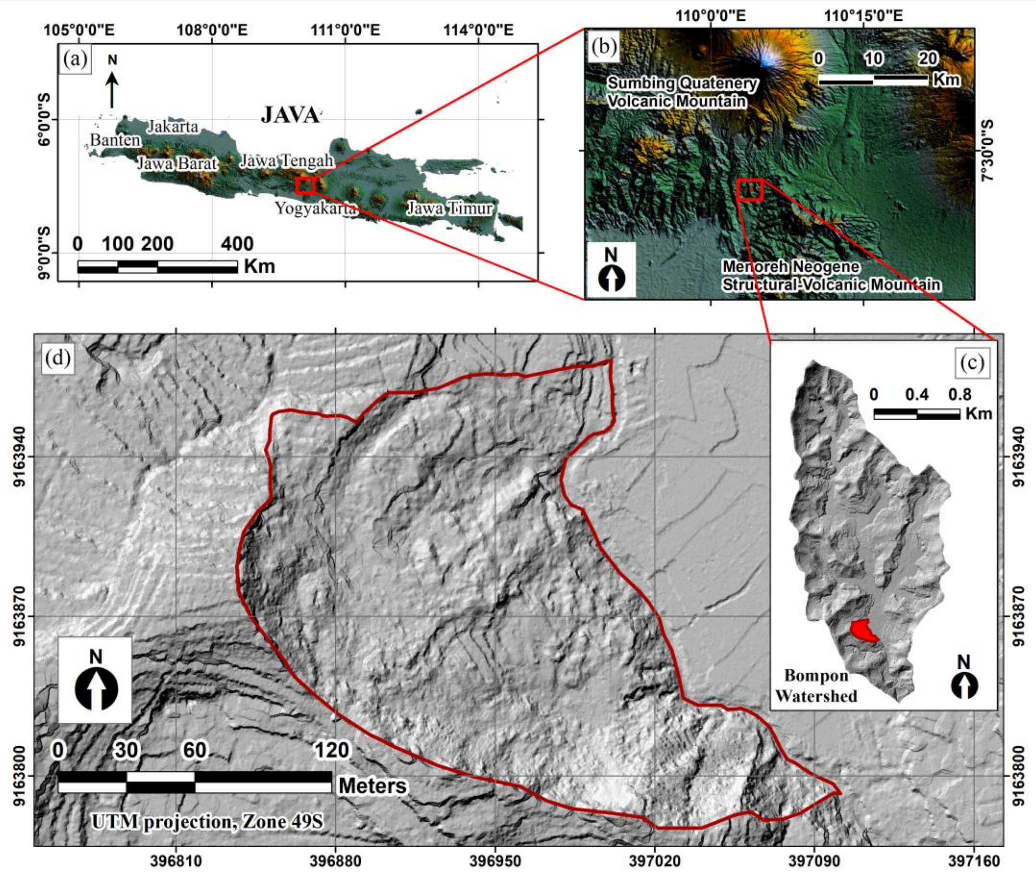

Figure 1: Study area: (a) Java Island, the red rectangle shows the area between Sumbing volcano and the Menoreh mountains, (b) Digital Elevation Model (DEM) of the area between Sumbing volcano and the Menoreh mountains, (c) Bompon sub-watershed, and (d) Kalisari landslide

All spatial data, including LiDAR point clouds, GNSS measurements, and ERT electrode positions, were referenced to the Universal Transverse Mercator (UTM) coordinate system, Zone 49S, WGS84 datum. A standard compass and clinometer were used for manual measurements of tree stem-lean angles and azimuths as validation data.

2.2 Methods

The methodology of this study integrates three complementary datasets, comprising GNSS positioning, ERT, and UAV-LiDAR, into a comprehensive workflow (Figure 2). GNSS provided a common georeferencing framework for both the geophysical and the remote-sensing data. The ERT pipeline produced two-dimensional resistivity sections to characterize the subsurface and infer the slip surface. The UAV-LiDAR pipeline derived surface morphology from ground points and stem-lean metrics from non-ground points. The outputs of all three streams were then co-registered in a GIS. The UAV-LiDAR products, the stem-lean vectors, and the inverted ERT sections were georeferenced to a common projected coordinate system (UTM Zone 49S, WGS84). This shared reference allowed anomalies from each dataset to be compared at identical georeferenced locations. The cross-comparison is therefore spatial in nature, supported by direct field observation of surface cracks.

2.2.1 Surface morphology analysis and stem lean estimation

The UAV-LiDAR survey covered the entire landslide body, including the source, transport, and accumulation zones. LiDAR point cloud data were classified into ground and non-ground points using CloudCompare [25]. Ground points were interpolated into a high-resolution digital terrain model (DTM), from which hillshade and morphometric parameters were derived [26]. Non-ground points were used for stem-lean analysis, a dendrogeomorphological technique that uses the angle and direction of tree-trunk inclination as a proxy for ground deformation [14][15] and [16]. As slopes move, trees respond through compensatory growth and tilting, which records cumulative deformation over time. This technique was used here to identify the most active zones within the landslide.

Individual tree detection and height measurement were prerequisite steps for stem-lean estimation, not primary objectives of this study. Detecting individual trees avoided ambiguity from multi-stemmed trees and overlapping canopies in identifying the true stem axis [27] and [28]. The stem-lean extraction followed four main steps. First, individual trees were manually segmented from the non-ground points using CloudCompare, producing 175 trees. Only trees with a single, clearly defined stem were kept, and shrubs were excluded (Figure 3(a) and (b)). All further processing was carried out in Python (NumPy, pandas, SciPy, GeoPandas) in Google Colab. The complete source code used in this study is available at https://github.com/Rafijuliasgeoinfo/stem-lean-uav-lidar. Second, the height above ground (HAG) was computed for each point and rescaled to a 0–1 range, called the normalized height (HN). This step separated the lower, middle, and upper parts of each stem. Third, the stem axis was estimated for each tree. The stem axis is the three-dimensional line that represents the orientation of the trunk. Two complementary algorithms were used to fit this line. The TRUNK algorithm fits a line through the lower stem points using Random Sample Consensus (RANSAC) and refines it with principal component analysis (PCA) to follow the main trunk direction [27][28] and [29]. The EXTREME algorithm instead draws the line between the base and the top of the stem, then filters it with PCA to reduce noise [30]. Finally, the lean angle and lean azimuth were computed from the fitted stem axis.

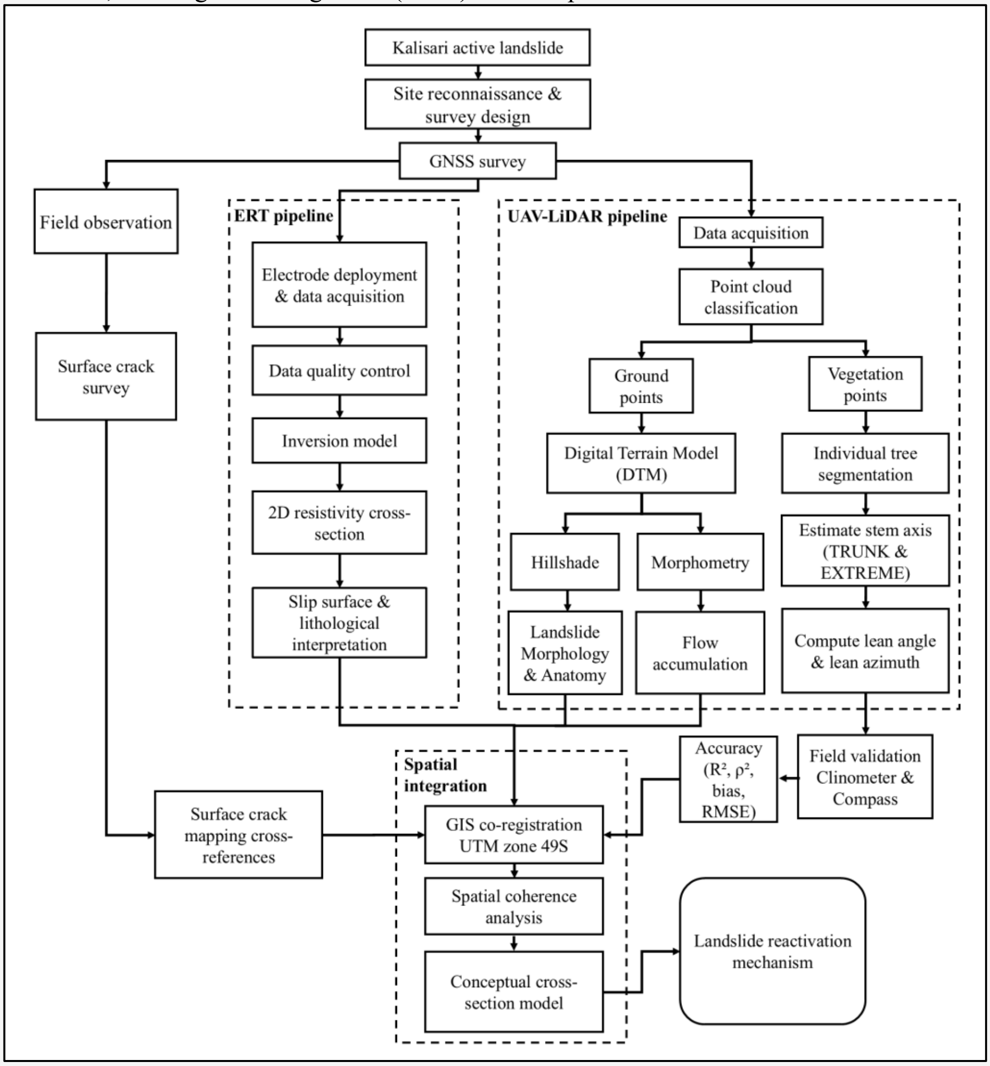

Figure 2: Integrated UAV-LiDAR and ERT workflow for the Kalisari landslide, with GNSS providing georeferencing for both pipelines

ISSN: 1686-6576 (Printed) | ISSN 2673-0014 (Online) | © Geoinformatics International

The resulting stem axis vector $\mathrm{v} = (v_x, v_y, v_z)$ was normalized and constrained to point upward ($v_z > 0$). The stem lean angle was defined as the deviation from the vertical [29] and [31] using Equation 1:

$$\theta = \arccos(\frac{| v_z |}{\| \mathrm{v} \|})$$

Equation 1

Where:

θ = stem lean angle (°)

v_z = vertical component of the stem axis vector

$\| \mathrm{v} \|$ = magnitude of the stem axis vector, calculated as $\| \mathrm{v} \| = \sqrt{v_x^2 + v_y^2 + v_z^2}$

v = stem axis vector (v_x, v_y, v_z)

v_x = x-component of the stem axis vector

v_y = y-component of the stem axis vector

The lean azimuth was calculated from the horizontal projection (v_x, v_y) using the four-quadrant atan2 function [32] as shown in Equation 2:

$$\alpha^* = \mathrm{atan2}(v_y, v_x)$$

Equation 2

Where:

α^* = preliminary lean azimuth angle

α = final stem lean azimuth angle (0–360°)

v_x = x-component of the stem axis vector

v_y = y-component of the stem axis vector

The preliminary azimuth α^* was converted from radians to degrees. The resulting angle was then normalized to the range 0–360° to obtain the final stem lean azimuth (α), representing the dominant lean direction in the horizontal plane. Both algorithms were applied to each tree, and the final solution was selected through visual quality control (QC). The consistency between vectors and stems was checked in the three-dimensional point cloud view (Figure 3(a) and (b)).

The reliability of the method was assessed by comparing LiDAR-derived stem-lean estimates with field measurements. The validation sample consisted of 52 trees distributed across the entire landslide body, representing the main elements of the landslide anatomy. Performance was evaluated using R^2, bias, and RMSE, three metrics that are widely used for the evaluation of environmental models [33]. We also report ρ^2, the square of the Jammalamadaka–Sengupta circular correlation coefficient. This statistic is a circular analogue of R^2 and measures the directional agreement between LiDAR-derived and field-measured stem-lean azimuths [34]. All derived morphology products, flow-accumulation paths, and stem-lean vectors were georeferenced and analyzed spatially in a geographic information system (GIS).

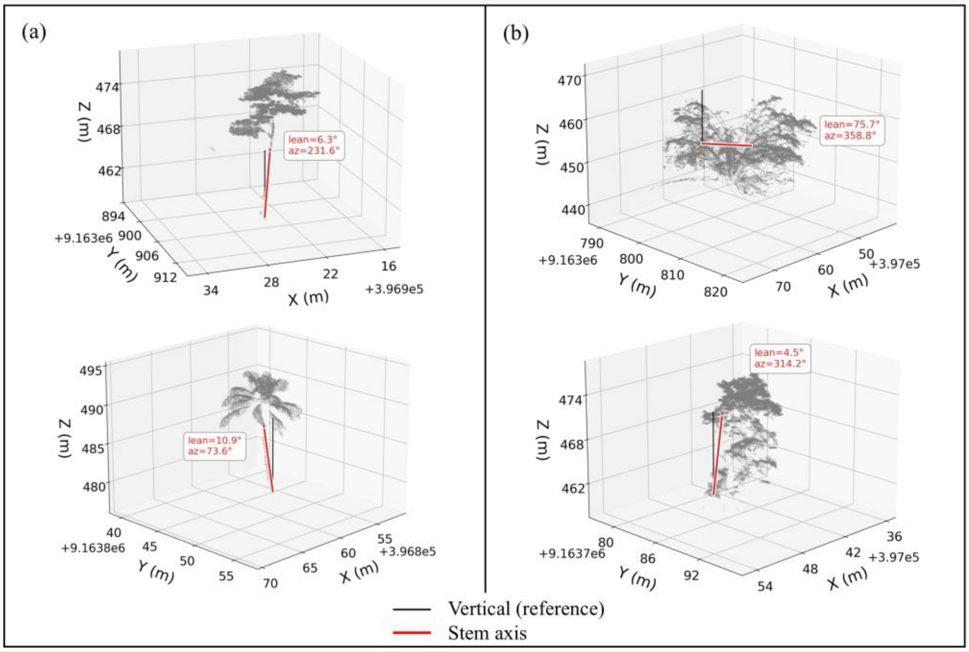

Figure 3: Three-dimensional visualization of tree stem lean for data selection and result QC (a) usable point cloud, where individual stems are clearly visible, (b) point cloud that cannot be used because stems are not clearly visible and the vegetation appears as shrubs or dense clumps

ISSN: 1686-6576 (Printed) | ISSN 2673-0014 (Online) | © Geoinformatics International

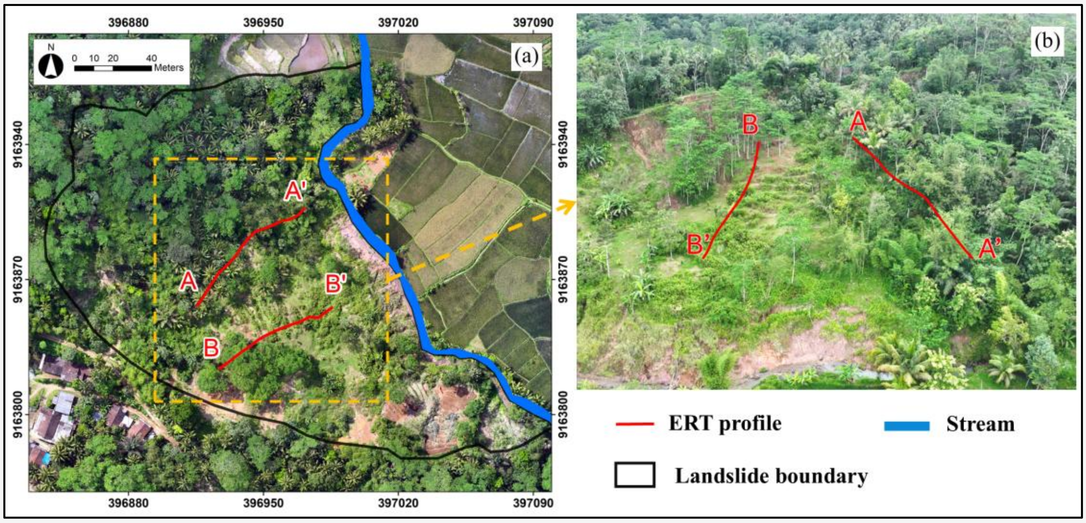

Figure 4: Location of electrical resistivity profiles visualized from: (a) orthophoto aerial image and (b) oblique view

2.2.2 ERT data analysis

Electrical resistivity tomography is particularly suited to volcanic soil contexts. Saturated, clay-rich material has markedly lower resistivity than drier, coarser material. This contrast allows clear identification of zones prone to failure. ERT can therefore detect the saturated and structurally weak zones that often drive landslide activity in volcanic terrain [20] and [21]. Two-dimensional ERT surveys were carried out along two profiles (A and B) that cross the head and main body of the landslide (Figure 4). Two-dimensional ERT was selected for several reasons. It provides sufficient resolution to characterize subsurface structure along strategically oriented profiles. It also requires substantially less field time, equipment, and computational resources than three-dimensional surveys. This approach is consistent with established practice in landslide investigation [19][20] and [21]. A dipole–dipole configuration was used with two electrode spacing sets on each profile. The combination of the two sets was chosen to obtain detailed lateral resolution and sufficient penetration depth. The first set used a base spacing of a = 1 m with separation factor n = 1–8, whereas the second set used a = 4 m with n = 2–6 to reduce sensitivity overlap and extend the depth range (pseudo depth).

ERT data were corrected for position and topography, and then processed and inverted using ResIPy [35]. The inversion used an Occam type smoothness constrained least squares scheme [36]. The goal was to obtain a two-dimensional log resistivity model that reproduces the apparent resistivity data within the limits of measurement uncertainty. The quality of the inversion results was evaluated using the normalized root mean square (RMS) misfit and the stability of model changes between iterations [37]. The final model was selected when the RMS was in a low and stable range (1–2) and the resistivity pattern was consistent with field observations [38]. The inversion results were then interpreted qualitatively and spatially. Vertical and lateral patterns of resistivity contrast were compared with slope morphology and the distribution of stem lean to identify actively reactivating landslide zones.

3. Results

3.1 Surface Characteristics of the Landslide

High-resolution surface morphology analysis reveals that the Kalisari landslide is a complex rotational failure. It is characterized by heterogeneous retrogressive movements. Along the western and southwestern flanks, a concave and arcuate main scarp is well developed. In the northern sector, a series of discontinuous minor scarps indicates active headward retrogression. The central landslide body is dominated by rotated soil blocks and hummocky topography. The landslide toe shows signs of active compression and bulging directed toward the nearby river (Figure 7(a)). A network of erosional gullies also incises the failed mass. These gullies mark preferential surface water flow paths that route runoff toward the interior of the landslide.

3.2 Validation and Analysis of Vegetation Deformation Patterns

3.2.1 Validation of stem lean

The extraction method was validated against 52 field-measured trees. These trees were distributed across the main anatomical elements of the landslide. For stem-lean angle, the coefficient of determination reaches R^2 = 0.87. This indicates that the model

ISSN: 1686-6576 (Printed) | ISSN 2673-0014 (Online) |

explains most of the variance in field measurements. The bias is 1.4° and the RMSE is 3.9° (Figure 5(a)). Validation of lean azimuth also shows strong directional agreement. The circular correlation coefficient reaches $\rho^2 = 0.85$, with a bias of 7.7° and an RMSE of 19.7° (Figure 5(b)). These results confirm that LiDAR-derived stem-lean metrics are an accurate and reliable proxy for mapping active slope deformation.

3.2.2 Spatial pattern of vegetation deformation

The spatial distribution of the 175 analyzed trees reveals highly ordered, non-random patterns of slope movement. The highest frequency occurs in the gentle lean class of 5 to 10 degrees, with over 50 trees. The lowest frequency is found in the extreme lean class exceeding 60 degrees (Figure 6(a)).

Trees with stem-lean angles above 20 degrees are tightly clustered along active deformation zones. These zones include main scarps, sharp slope breaks, and the compressive landslide toe (Figure 7(b)). The lean azimuth analysis shows a well-organized directional distribution. The dominant pattern is unimodal, oriented toward the northeast and east between 45 and 100 degrees (Figure 6(b)). This matches the primary downslope mass movement vector. The highest concentration falls in the east to southeast sector between 70 and 100 degrees, accounting for 10 to 12 percent of all trees. A secondary contribution from the northeast to east sector between 45 and 70 degrees accounts for approximately 6 to 9 percent. Western to northwestern directions are almost absent at less than 5 percent.

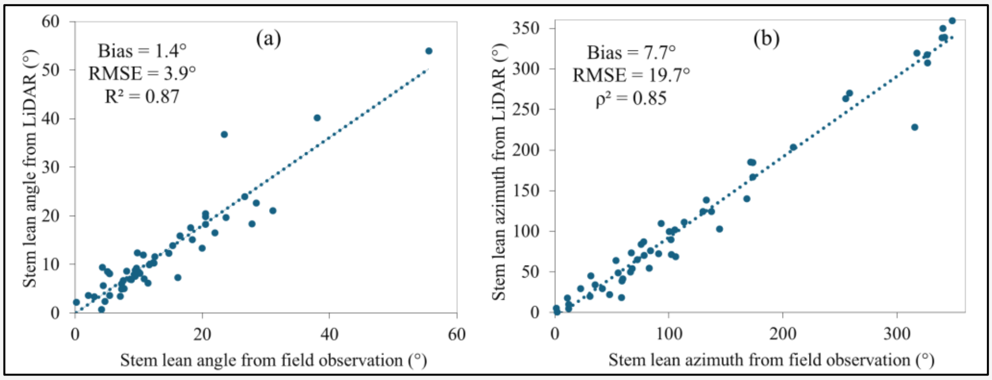

Figure 5: Scatter plots of: (a) stem lean angle from LiDAR versus field observations and (b) stem lean azimuth from LiDAR versus field observations

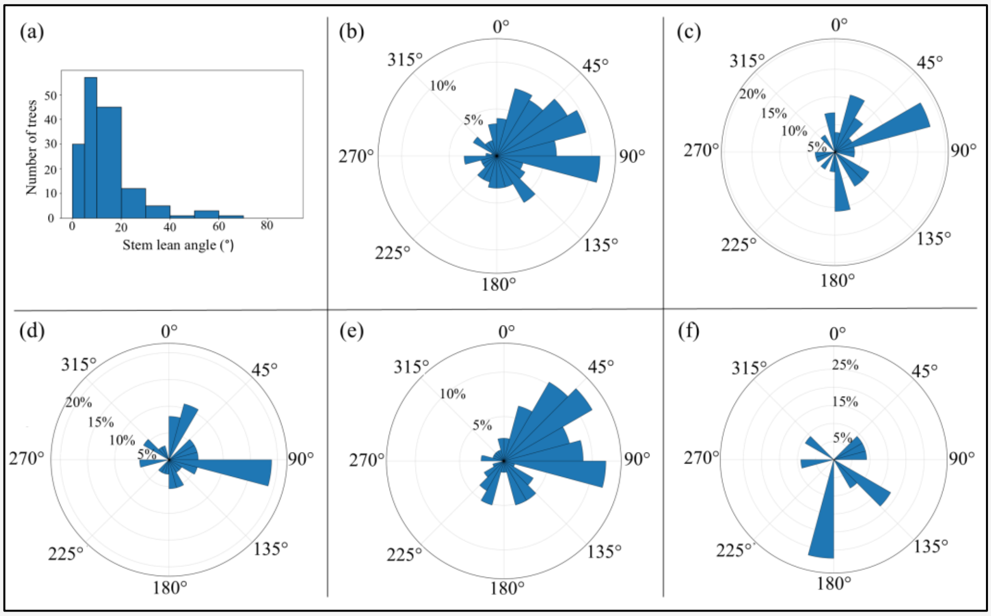

Figure 6: (a) Histogram of the distribution of mean stem lean angle on the Kalisari landslide. Rose plots of stem lean azimuth (b) all trees analyzed and, for each part of the landslide anatomy, (c) landslide crown, (d) landslide head, (e) landslide body, and (f) landslide toe. A value of 0° indicates north

ISSN: 1686-6576 (Printed) | ISSN 2673-0014 (Online) |

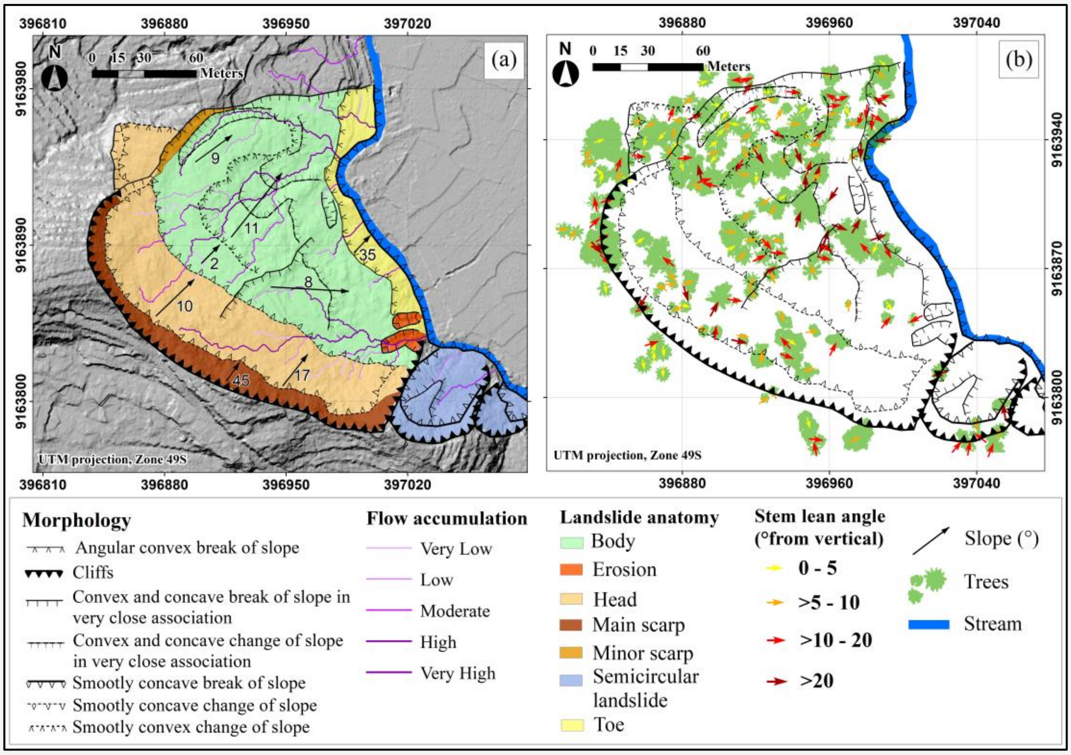

Figure 7: (a) Landslide anatomy and morphology,
(b) map of tree stem lean over the Kalisari landslide morphology

Zone-by-zone analysis clarifies localized movement dynamics. The landslide crown shows a highly dispersed lean pattern between 0 and 180 degrees (Figure 6(c)). At the landslide head, localized upslope back-tilting is observed in several trees. The dominant direction, however, remains eastward between 90 and 100 degrees (Figure 6(d)). The landslide toe shows a clear directional shift. Lean vectors fan out toward the south at 180 degrees and southeast at 135 degrees. This pattern indicates compression and material spreading at the slope base (Figure 6(f)). The landslide body displays the most coherent pattern. Most trees lean consistently toward the northeast to southeast sector between 45 and 135 degrees. This confirms unified translational block movement (Figure 6(e)).

3.3 Subsurface Characteristics

3.3.1 Two-dimensional resistivity sections

The two-dimensional inversion models achieved low normalized RMS misfit values. Profile A recorded 1.04 and Profile B recorded 1.20. These values confirm that the resistivity models are stable and reliable for geological interpretation. The inverted sections reveal a highly heterogeneous subsurface structure. Resistivity values range from 3 to 1000 Ω·m (Figure 8(b) and 8(c)).

Profile A is dominated by very low resistivity zones between 3 and 30 Ω·m. These appear as distinct blue pockets in the central and lower sectors of the section. They indicate moist to water-saturated clay-rich material. Near the surface, high-resistivity zones between 90 and 1000 Ω·m are also present. These represent drier soils or open fissures. Profile B shows a similar subsurface pattern. It is characterized by a higher proportion of intermediate resistivity values between 30 and 90 Ω·m. Discrete low-resistivity pockets between 3 and 30 Ω·m remain present. A very high resistivity anomaly exceeding 1000 Ω·m occurs in the deeper lower slope sector. This is interpreted as competent altered breccia bedrock (Table 1). Two primary resistivity zones are identified consistently across both profiles. The first is the seepage fissure zone (SF). It corresponds to blue-colored areas between 3 and 30 Ω·m forming continuous layers in the central to lower sections. SF is interpreted as saturated throughflow pathways and potential slip surfaces. The second is the dry fissure zone (DF). It corresponds to near-surface values greater than 600 Ω·m, shown in orange and red. DF zones frequently overlie the weaker SF zones (Figure 8(c)).

ISSN: 1686-6576 (Printed) | ISSN 2673-0014 (Online) | © Geoinformatics International

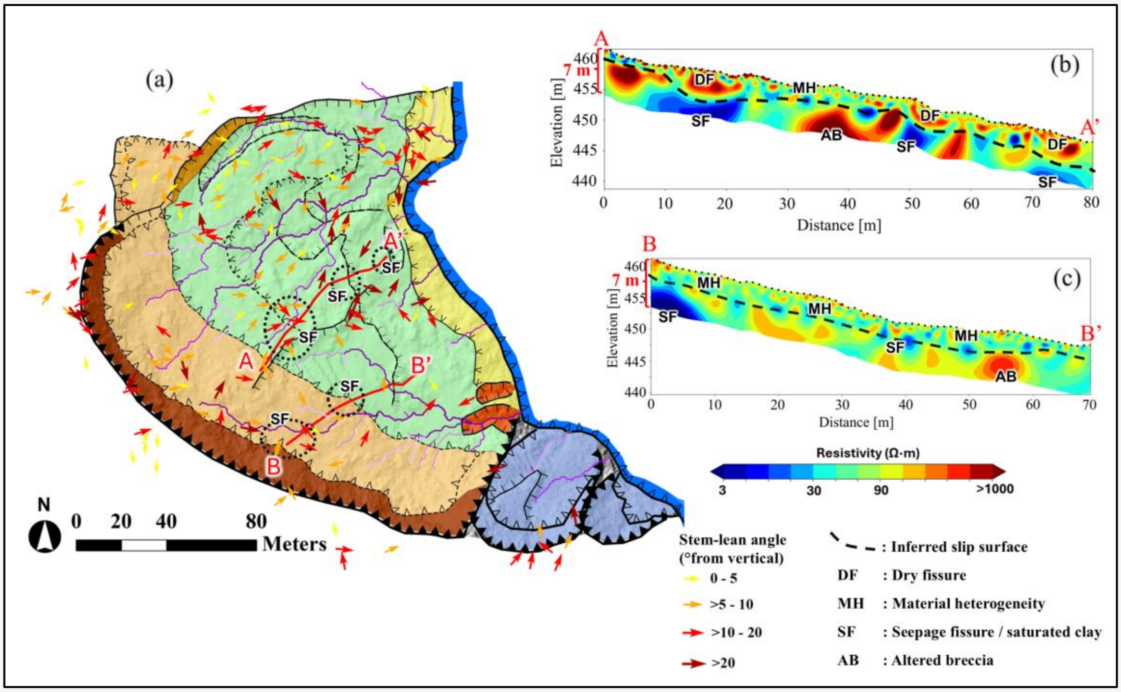

Figure 8: (a) Landslide anatomy, morphology, and stem-lean. (b) two-dimensional resistivity section along profile A. (c) two-dimensional resistivity section along profile B

Table 1: Resistivity values and lithological interpretation of the Kalisari landslide

Resistivity (Ω·m)	Dominant soil characteristics	Interpretation for thick-soil landslide
3–30	Saturated clay, locally with fractures filled with water	Potential slip-surface zone. When excessively saturated, it can become the slip surface in very thick soils. At the surface it appears as seepage lines. In the subsurface it corresponds to throughflow pathways.
30–90	Material more resistant than the 3–30 Ω·m class, transitional around the saturated clay	Boundary between layers, heterogeneous material.
90–1000	Relatively drier / coarser soil, many roots, locally fractures filled with air	Thin lateral variations influenced by vegetation/roots and fractures. Not the main weak zone, but it can act as an entry point for water. Relatively resistant material or fractures that often hang above the saturated zone.
>1000	Altered breccias	Altered breccias located below the soil surface.

3.4 Spatial Integration of Surface and Subsurface Features

Spatial integration of surface morphology and subsurface anomalies reveals strong coherence across all datasets (Figure 8(a) and (c)). The SF zone is not randomly distributed across the slope. It occurs directly beneath surface tension cracks linked to DF zones. It also occurs along the primary axes of surface flow accumulation (Figure 9(a) and (b)). Along Profile A, the SF zone closely coincides with structural surface cracks (Figure 9(a)). Along Profile B, it aligns with surface drainage accumulation pathways (Figure 9(b)). Field observations validate these patterns. Ground discontinuities and active water seepage are present in the central and toe sectors, downstream of the mapped accumulation lines. This spatial correspondence indicates that preferential water infiltration through surface discontinuities recharges the weak saturated clay layer. This is likely the primary mechanism driving rapid slope destabilization.

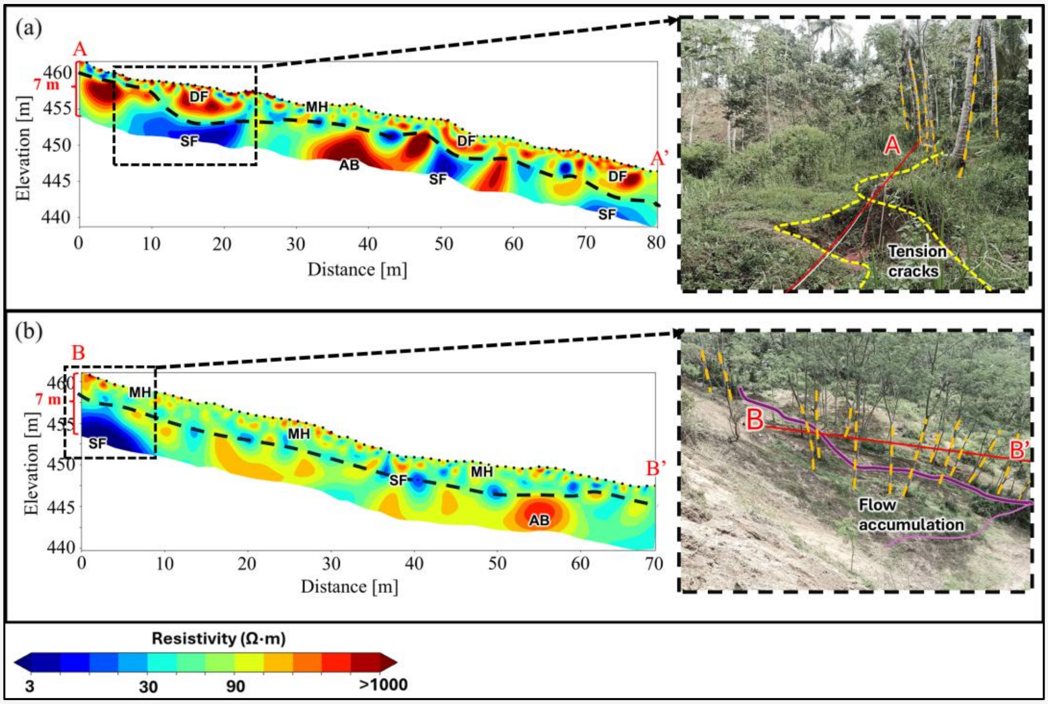

Figure 9: (a) Saturated zone (SF) located beneath surface cracks (DF) and (b) saturated zone (SF) located beneath surface flow accumulation paths

4. Discussion

4.1 LiDAR-Derived Stem Lean as a Deformation Proxy

The integration of UAV-LiDAR and ERT provides a deeper understanding of the mechanisms of the active landslide in Kalisari. This combined approach goes beyond what each method can achieve on its own. Together, LiDAR and ERT reveal critical relationships between surface conditions and the main controlling factors at depth. Within this integrated framework, vegetation anomalies serve as a highly responsive surface expression of the underlying geomechanical changes.

A key contribution of this study is the validation and application of stem-lean analysis as a biosensor. The validation shows high statistical performance. Stem-lean metrics extracted from LiDAR are a reliable proxy for tree deformation and for actual field conditions. This is important because it shifts the use of stem lean from a qualitative observation to a quantitative metric. Our data show that stem-lean patterns are not random. Stems predominantly lean toward the east, in line with the direction of downslope mass movement. This supports the view that slope deformation is a directed and coherent process rather than a random motion [39]. As highlighted in dendrogeomorphological studies, trees act as natural long-term recorders of slope deformation [40] and [41].

Our work extends this understanding by showing that the spatial pattern of stem lean can be used to diagnose specific movement mechanisms in different parts of the landslide anatomy. In most sectors of the landslide, stems lean downslope, while the toe shows a fanning pattern that clearly indicates a zone of compression and material accumulation [42] and [43]. Stem-lean analysis therefore not only demonstrates that the slope is still deforming, but also provides information on the dominant direction and mechanisms of mass movement [15][16] and [44].

The accuracy of the stem-lean results can be explained by the data geometry. The lean angle was resolved more accurately than the lean azimuth. This contrast reflects how each metric is measured, not a flaw in the method. The angle depends on the vertical contrast between the stem and the ground, which dense LiDAR point clouds capture well. The azimuth is less stable when the lean angle is small, because a nearly vertical stem has no well-defined horizontal direction [29] and [34]. Even so, the strong circular correlation of the azimuth confirms that the dominant lean directions remain reliable for diagnosing movement. The reliability of vegetation-based indicators in this study is supported by the internal consistency of the data. If non-landslide factors had dominated the stem-lean signal, the lean directions would be expected to scatter. Instead, the azimuth distribution is highly organized and unimodal (ρ^2 =

ISSN: 1686-6576 (Printed) | ISSN 2673-0014 (Online) |

0.85), and it aligns closely with the independent downslope movement direction inferred from morphology and ERT. This agreement indicates that the stem-lean signal at Kalisari is governed mainly by ground deformation. Even so, vegetation responds to ground movement indirectly.

4.2 Landslide Kinematics

Previous research established the rotational character of the Kalisari landslide [20]. However, our findings indicate that the current deformation cycle is dominated by translational components and downslope creep, even though the slope morphology still exhibits rotational features. Similar patterns have been reported on many mountain slopes, where older rotational scarps remain visible at the surface. These scarps are overlain by younger translational blocks that repeatedly move along the same slip surface [45] and [46]. This dominant lateral movement refers to the direction and pattern of the present deformation, not to a measured displacement rate. The interpretation rests on the coherent stem-lean azimuths (Figure 6(b)) and the sub-horizontal, slope-parallel slip surface geometry delineated in the ERT profiles (Figure 8(b) and (c)), rather than on direct measurement of displacement magnitude. The rate of movement was not quantified, as the survey represents a single point in time. Stem-lean data show that the present movement is a slow, directed block slide rather than the large-scale rotation that occurred during the initial failure phase [9]. The motion is now predominantly translational. This explains why the landslide head is no longer dominated by trees that lean upslope (back-tilting). Instead, it shows a relatively uniform eastward lean that follows the average movement vector of the landslide body.

4.3 Interpretation of Subsurface Resistivity Structures

The ERT results can be explained by the physical properties of the subsurface materials. The low-resistivity zone (3–30 Ω·m) coincides with saturated, clay-rich material. Saturated clay is both mechanically weak and electrically conductive. It therefore appears as a low-resistivity anomaly and, at the same time, acts as a potential slip surface [20] and [47]. This dual role explains why the low-resistivity zone is a primary control on reactivation. Its spatial agreement with surface cracks and flow-accumulation paths further indicates that infiltrating water recharges this weak layer [48][49] and [50].

The main strength of this integrated methodology is its ability to link surface controlling factors with subsurface response. We find strong evidence that zones of surface flow accumulation, slope breaks, and surface cracks act as primary conduits that route rainfall into the ground [48]. This water then infiltrates directly into the saturated clay layer identified by ERT [49] and [50]. This mechanism explains why the slope can become highly unstable within a short time after intense rainfall [51]. The interpretation of the low-resistivity zone (3–30 Ω·m) as saturated, clay-rich material is well supported. It is consistent with prior geoelectrical and geological investigations in the same and geologically similar thick-soil landslides of the region [20] [21] and [47]. This regional grounding reduces interpretive ambiguity. Even so, resistivity values can still vary with porosity, mineralogy, and moisture content.

The subsurface characterization used two-dimensional ERT profiles rather than a three-dimensional survey. This choice reflects both methodological suitability and field conditions. A 3D survey depends on dense interpolation and prediction between profiles. In heterogeneous thick-soil terrain, this process can introduce artefacts and spatial distortion. Such distortion complicates the interpretation. The target of this study is a slip surface. A slip surface is more complex and discrete than a continuous groundwater body. It is therefore better resolved by high-resolution 2D cross-sections. This approach is also consistent with previous landslide investigations in similar thick-soil settings. In addition, the Kalisari landslide has an elongated form along its main movement direction. 2D profiles capture this form effectively. The steep and densely vegetated slope also limits the electrode array length and the survey time that are practical in the field. The two profiles were therefore positioned across the head and main body, where reactivation is most active.

ERT resolution decreases with depth, so deeper features are imaged less sharply than shallow ones. This constraint does not weaken the present conclusions. As described above, the active movement at Kalisari is concentrated along a shallow, near-surface slip zone. The ERT interpretation therefore focuses on the shallow to intermediate depths, where resolution is highest and where the active weak layer is located. Greater depths, which carry higher uncertainty, fall outside the scope of this interpretation. Two measures keep the shallow interpretation reliable. Each profile combined two electrode spacings to balance lateral detail with penetration depth. The resistivity patterns were also compared with field observations of cracks and seepage.

4.4 Limitations and Future Perspectives

This study has several limitations that also define clear directions for future work. The stem-lean

ISSN: 1686-6576 (Printed) | ISSN 2673-0014 (Online) | © Geoinformatics International

metric would benefit from field ground-checking of individual trees, for example by relating root orientation and anchoring to the observed lean direction. The ERT interpretation was not verified by boreholes, and direct drilling would confirm the saturated weak layer inferred from the resistivity sections. Both datasets would also benefit from multi-temporal monitoring. Repeated UAV-LiDAR and ERT surveys would add a temporal dimension, allowing the rate of reactivation to be quantified and the rainfall-driven mechanism to be tested directly. These directions build on the present results and would extend the approach toward continuous, transferable landslide monitoring in volcanic terrains. Understanding this hydromechanical mechanism has direct implications for landslide mitigation. We recommend upstream hydrological control through surface water management. This includes constructing drainage channels along LiDAR-mapped flow-accumulation paths to intercept rainfall before it infiltrates into the weak layer [52], and actively sealing ground cracks. This approach can be complemented by shallow subsurface drainage to intercept throughflow [53]. Such data-driven mitigation strategies provide an effective and sustainable way to maintain long-term stability in landscapes underlain by thick volcanic soils.

5. Conclusions

This study provides detailed insight into reactivation mechanisms at the Kalisari active landslide. Although the overall morphology is rotational, the landslide behavior varies across the landslide anatomy. UAV-LiDAR analysis indicates coherent lateral displacement in the head and body, whereas the toe is characterized by compressional deformation and material accumulation. These surface-based inferences are supported by ERT results, which delineate low-resistivity zones interpreted as saturated weak materials. The low-resistivity zones spatially coincide with surface cracks, flow-accumulation pathways, and clusters of trees exhibiting high stem-lean angles. Overall, the combined UAV-LiDAR and ERT approach offers an effective framework for mapping reactivation zones and linking surface deformation signals with subsurface structure in volcanic terrains. This integration further highlights the potential of vegetation-derived deformation metrics as quantitative indicators of landslide instability and provides a stronger basis for targeted mitigation planning.

Several directions remain for future research to build upon the integrated framework established in this study. The vegetation-based signal could be strengthened by relating stem-lean directions to in-situ root orientation, and the geophysical weak layer could be confirmed by subsurface drilling. The analysis is also based on a single observation in time, so time-series measurements are required to capture how fast the movement progresses. Once validated, the integrated workflow could be applied to other landslides in similar volcanic terrains. This study also supports several Sustainable Development Goals. It contributes to disaster risk reduction and resilient communities (SDG 11) and to the protection of mountain ecosystems (SDG 15). The approach further shows that meaningful landslide diagnostics can be achieved with accessible UAV and vegetation-based methods. We hope this encourages younger researchers to develop low-cost monitoring tools for hazard-prone regions.

Acknowledgements

The authors would like to thank Sitibecik Co. for their logistical and technical support, which played an important role in enabling the implementation of this study. The authors also express their sincere appreciation to Transbulent Research Group for their assistance in providing supporting data for this research.

References

[1] Korup, O., (2006). Effects of Large Deep-Seated Landslides on Hillslope Morphology, Western Southern Alps, New Zealand. *Journal of Geophysical Research: Earth Surface*, Vol. 111(F2). https://doi.org/10.1029/2004JF000242.

[2] McColl, S. T., Holdsworth, C. N., Fuller, I. C., Todd, M. and Williams, F., (2022). Disproportionate and Chronic Sediment Delivery from a Fluvially Controlled, Deep-Seated Landslide in Aotearoa New Zealand. *Earth Surface Processes and Landforms*, Vol. 47(8); 1972–1988. https://doi.org/10.1002/esp.5358.

[3] Noviyanto, A., Sartohadi, J. and Purwanto, B. H., (2020). The Distribution of Soil Morphological Characteristics for Landslide-Impacted Sumbing Volcano, Central Java-Indonesia. *Geoenvironmental Disasters*, Vol. 7(1). https://doi.org/10.1186/s40677-020-00158-8.

[4] Indrawan, I. G. B., Tamado, D., Abrar, M. and Warmada, I. W., (2024). Mineralogical and Engineering Properties of Soils Derived from in Situ Weathering of Tuff in Central Java, Indonesia. *Geosciences*, Vol. 14(8). https://doi.org/10.3390/geosciences14080213.

ISSN: 1686-6576 (Printed) | ISSN 2673-0014 (Online) | © Geoinformatics International

[5] Sarah, D., Zulfahmi, Z., Putra, M. H. Z., Madiutomo, N., Gunawan, G., Sumaryadi, S. and Ahmid, D. A., (2024). Back Analysis of Rainfall-Induced Landslide in Cimanggung District of Sumedang Regency in West Java Using Deterministic and Probabilistic Analyses. *Geosciences*, Vol. 14(12). https://doi.org/10.3390/geosciences14120347.

[6] Morelli, S., Pazzi, V., Frodella, W., Nocentini, M., Casagli, N. and Fanti, R., (2018). Kinematic Reconstruction of a Deep-Seated Gravitational Slope Deformation: Insights into the Role of Fluvioglacial Deposits on Slope Evolution. *Geosciences*, Vol. 8(1). https://doi.org/10.3390/geosciences8010026.

[7] Rabus, B., Engelbrecht, J., Clague, J. J., Donati, D., Stead, D. and Francioni, M., (2022). Response of a Large Deep-Seated Gravitational Slope Deformation to Meteorological, Seismic, and Deglaciation Drivers as Measured by InSAR. *Frontiers in Earth Science*, Vol. 10. https://doi.org/10.3389/feart.2022.918901.

[8] Saez, J. L., Corona, C., Stoffel, M., Schoeneich, F. and Berger, F., (2012). Probability Maps of Landslide Reactivation Derived from Tree-Ring Records: Pra Bellon Landslide, Southern French Alps. *Geomorphology*, Vol. 138(1); 189–202. https://doi.org/10.1016/j.geomorph.2011.08.034.

[9] Massey, C. I., Petley, D. N. and McSaveney, M. J., (2013). Patterns of Movement in Reactivated Landslides. *Engineering Geology*, Vol. 159; 1–19. https://doi.org/10.1016/j.enggeo.2013.03.011.

[10] Trepekli, K., Balstrøm, T., Friborg, T., Fog, B., Allotey, A. N., Kofie, R. Y. and Møller-Jensen, L., (2022). UAV-Borne, LiDAR-Based Elevation Modelling: A Method for Improving Local-Scale Urban Flood Risk Assessment. *Natural Hazards*, Vol. 113; 423–451. https://doi.org/10.1007/s11069-022-05308-9.

[11] Choi, S. K., Ramirez, R. A. and Kwon, T. H., (2023). Acquisition of High-Resolution Topographic Information in Forest Environments using Integrated UAV-LiDAR System: System Development and Field Demonstration. *Heliyon*, Vol. 9(9). https://doi.org/10.1016/j.heliyon.2023.e20225.

[12] Jaboyedoff, M., Oppikofer, T., Abellán, A., Derron, M. H., Loye, A., Metzger, R. and Pedrazzini, A., (2012). Use of LIDAR in Landslide Investigations: A Review. *Natural Hazards*, Vol. 61(1); 5–28. https://doi.org/10.1007/s11069-010-9634-2.

[13] Pratiwi, E. S., Shen, S. M. and Sartohadi, J., (2024). Understanding the Nature of Landslides through Detailed Geomorphological Mapping on the Sumbing Volcanic Landscape, Java Island, Indonesia. *Journal of Maps*, Vol. 20(1). https://doi.org/10.1080/17445647.2024.2429710.

[14] Malik, I. and Wistuba, M., (2012). Dendrochronological Methods for Reconstructing Mass Movements: An Example of Landslide Activity Analysis Using Tree-Ring Eccentricity. *Geochronometria*, Vol. 39(3); 180–196. https://doi.org/10.2478/s13386-012-0005-5.

[15] Šilhán, K., (2015). Can Tree Tilting Indicate Mechanisms of Slope Movement?. *Engineering Geology*, Vol. 199; 157–164. https://doi.org/10.1016/j.enggeo.2015.11.005.

[16] Šilhán, K., (2021). Dendrogeomorphology of Different Landslide Types: A Review. *Forests*, Vol. 12(3). https://doi.org/10.3390/f12030261.

[17] Weidner, L., van Veen, M., Lato, M. and Walton, G., (2021). An Algorithm for Measuring Landslide Deformation in Terrestrial Lidar Point Clouds Using Trees. *Landslides*, Vol. 18(11); 3547–3558. https://doi.org/10.1007/s10346-021-01723-4.

[18] Chen, B., Maurer, J. and Gong, W., (2025). Applications of UAV in Landslide Research: A Review. *Landslides*, Vol. 22; 3029–3048. https://doi.org/10.1007/s10346-025-02547-2.

[19] Perrone, A., Lapenna, V. and Piscitelli, S., (2014). Electrical Resistivity Tomography Technique for Landslide Investigation: A Review. *Earth-Science Reviews*, Vol. 135; 65–73. https://doi.org/10.1016/j.earscirev.2014.04.002.

[20] Samodra, G., Ramadhan, M. F., Sartohadi, J., Setiawan, M. A., Christanto, N. and Sukmawijaya, A., (2020). Characterization of Displacement and Internal Structure of Landslides from Multitemporal UAV and ERT Imaging. *Landslides*, Vol. 17(10); 2455–2468. https://doi.org/10.1007/s10346-020-01428-0.

[21] Purnamasari, A. N. C., Sartohadi, J. and Hartantyo, E., (2024). Pseudo Sliding Plane in Super-Thick Soil Materials Deposit at Ngasinan Deep Landslide Area. *Revista Brasileira de Geomorfologia*, Vol. 25(2). https://doi.org/10.20502/rbgeomorfologia.v25i2.2540.

[22] Travelletti, J. and Malet, J. P., (2012). Characterization of the 3D Geometry of Flow-Like Landslides: A Methodology Based on the Integration of Heterogeneous Multi-Source Data. *Engineering Geology*, Vol. 128; 30–48. https://doi.org/10.1016/j.enggeo.2011.05.003.

[23] Sartohadi, J., Pulungan, N. A. H. J., Nurudin, M. and Wahyudi, W., (2018). The Ecological Perspective of Landslides at Soils with High Clay Content in the Middle Bogowonto Watershed, Central Java, Indonesia. *Applied and Environmental Soil Science,* Vol. 2018(1). https://doi.org/10.1155/2018/2648185.

[24] Pulungan, N. A. H. J. and Sartohadi, J., (2018). New Approach to Soil Formation in the Transitional Landscape Zone: Weathering and Alteration of Parent Rocks. *Journal of Environments*, Vol. 5(1); 1–7. https://doi.org/10.20448/journal.505.2018.51.1.7.

[25] Girardeau-Montaut, D., (2006). *Détection de changement sur des données géométriques tridimensionnelles*. Doctoral Dissertation. Télécom ParisTech, Palaiseau, France.

[26] Dewitte, O., Chung, C. J., Cornet, Y., Daoudi, M. and Demoulin, A., (2010). Combining Spatial Data in Landslide Reactivation Susceptibility Mapping: A Likelihood Ratio-Based Approach in W Belgium. *Geomorphology*, Vol. 122(1–2); 153–166. https://doi.org/10.1016/j.geomorph.2010.06.010.

[27] Reitberger, J., Schnörr, C., Krzystek, P. and Stilla, U., (2009). 3D Segmentation of Single Trees Exploiting Full Waveform LiDAR Data. *ISPRS Journal of Photogrammetry and Remote Sensing*, Vol. 64(6); 561–574. https://doi.org/10.1016/j.isprsjprs.2009.04.002.

[28] Lamprecht, S., (2015). *aTrunk – An ALS-Based Trunk Detection Algorithm*. Master's Thesis. Trier University, Germany. Available: https://www.uni-trier.de/fileadmin/fb6/prof/FER/Publikationen/Lamprecht_masters_thesis_aTrunk.pdf.

[29] Lamprecht, S., Stoffels, J. and Udelhoven, T., (2020). ALS as Tool to Study Preferred Stem Inclination Directions. *Remote Sensing*, Vol. 12(22). https://doi.org/10.3390/rs12223744.

[30] Wang, D., Song, Z., Miao, T., Zhu, C., Yang, X., Yang, T., Zhou, Y., Den, H. and Xu, T., (2023). DFSP: A Fast and Automatic Distance Field-Based Stem-Leaf Segmentation Pipeline for Point Cloud of Maize Shoot. *Frontiers in Plant Science*, Vol. 14. https://doi.org/10.3389/fpls.2023.1109314.

[31] Liang, X., Kankare, V., Hyyppä, J., Wang, Y., Kukko, A., Haggrén, H., Yu, X., Kaartinen, H., Jaakkola, A., Guan, F., Holopainen, M. and Vastaranta, M., (2016). Terrestrial Laser Scanning in Forest Inventories. *ISPRS Journal of Photogrammetry and Remote Sensing*, Vol. 115; 63–77. https://doi.org/10.1016/j.isprsjprs.2016.01.006.

[32] Yrttimaa, T., Kankare, V., Luoma, V., Junttila, S., Saarinen, N., Calders, K., Holopainen, M., Hyyppä, J. and Vastaranta, M., (2024). A Method for Identifying and Segmenting Branches of Scots Pine (*Pinus sylvestris* L.) Trees Using Terrestrial Laser Scanning. *Forestry: An International Journal of Forest Research*, Vol. 97(4); 531–545. https://doi.org/10.1093/forestry/cpad062.

[33] Bennett, N. D., Croke, B. F. W., Guariso, G., Guillaume, J. H. A., Hamilton, S. H., Jakeman, A. J., Marsili-Libelli, S., Newham, L. T. H., Norton, J. P., Perrin, C., Pierce, S. A., Robson, B., Seppelt, R., Voinov, A. A., Fath, B. D. and Andreassian, V., (2013). Characterising Performance of Environmental Models. *Environmental Modelling & Software*, Vol. 40; 1–20. https://doi.org/10.1016/j.envsoft.2012.09.011.

[34] Jammalamadaka, S. R. and SenGupta, A., (2001). *Topics in Circular Statistics*. World Scientific, Singapore. https://doi.org/10.1142/9789812779267.

[35] Blanchy, G., Saneiyan, S., Boyd, J., McLachlan, P. and Binley, A., (2020). ResIPy, an Intuitive Open-Source Software for Complex Geoelectrical Inversion/Modeling. *Computers & Geosciences*, Vol. 137. https://doi.org/10.1016/j.cageo.2020.104423.

[36] de Groot-Hedlin, C. and Constable, S., (1990). Occam's Inversion to Generate Smooth, Two-Dimensional Models from Magnetotelluric Data. *Geophysics*, Vol. 55(12), 1613–1624. https://doi.org/10.1190/1.1442813.

[37] Olayinka, A. I. and Yaramanci, U., (2000). Assessment of the Reliability of 2D Inversion of Apparent Resistivity Data. *Geophysical Prospecting*, Vol. 48(2); 293–316. https://doi.org/10.1046/j.1365-2478.2000.00173.x.

[38] Hermans, T. and Paepen, M., (2020). Combined Inversion of Land and Marine Electrical Resistivity Tomography for Submarine Groundwater Discharge and Saltwater Intrusion Characterization. *Geophysical Research Letters*, Vol. 47(3). https://doi.org/10.1029/2019GL085877.

[39] Stefanini, M. C., (2004). Spatio-Temporal Analysis of a Complex Landslide in the Northern Apennines (Italy) by Means of Dendrochronology. *Geomorphology*, Vol. 63(3–4); 191–202. https://doi.org/10.1016/j.geomorph.2004.04.003.

[40] Stoffel, M. and Bollschweiler, M., (2008). Tree-Ring Analysis in Natural Hazards Research: An Overview. *Natural Hazards and Earth System Sciences*, Vol. 8(2); 187–202. https://doi.org/10.5194/nhess-8-187-2008.

[41] Stoffel, M., Butler, D. R. and Corona, C., (2013). Mass Movements and Tree Rings: A Guide to Dendrogeomorphic Field Sampling and Dating. *Geomorphology*, Vol. 200; 106–120. https://doi.org/10.1016/j.geomorph.2012.12.017.

[42] Baron, I., Mikoš, M., Jemec, M., Ribičič, M. and Petkovšek, A., (2004). Structure and Dynamics of Deep-Seated Slope Failures in the Eastern Alps. *Natural Hazards and Earth System Sciences*, Vol. 4(3); 549–562. https://doi.org/10.5194/nhess-4-549-2004.

[43] Wistuba, M., Malik, I., Gärtner, H., Kojs, P. and Owczarek, P., (2013). Application of Eccentric Growth of Trees as a Tool for Landslide Analyses: The Example of Picea abies (L.) Karst. in the Carpathian and Sudeten Mountains (Central Europe). *Catena*, Vol. 111; 41–55. https://doi.org/10.1016/j.catena.2013.06.027.

[44] Šilhán, K., Tichavský, R., Fabiánová, A., Chalupa, V., Chalupová, O., Škarpich, V. and Tolasz, R., (2019). Understanding Complex Slope Deformation through Tree-Ring Analyses. *Science of the Total Environment*, Vol. 665; 1083–1094. https://doi.org/10.1016/j.scitotenv.2019.02.195.

[45] Pánek, T. and Klimeš, J., (2016). Temporal Behavior of Deep-Seated Gravitational Slope Deformations: A Review. *Earth-Science Reviews*, Vol. 156; 14–38. https://doi.org/10.1016/j.earscirev.2016.02.007.

[46] Osika, A., Wistuba, M. and Malik, I., (2018). Relief Evolution of Landslide Slopes in the Kamienne Mts (Central Sudetes, Poland) – Analysis of a High-Resolution DEM from Airborne LiDAR. *Contemporary Trends in Geoscience,* Vol. 7(1); 1–20. https://doi.org/10.2478/ctg-2018-0001.

[47] Purnamasari, A.N.C., Sartohadi, J. and Hartantyo, E., (2025). Electrical Resistivity Tomography and Seismic Refraction for Layer Identification in Super-Thick Soil in Landslide Area of Ngasinan, Purworejo, Indonesia. *Geosciences Journal*, Vol. 29(2); 274–289. https://doi.org/10.1007/s12303-025-00017-4.

[48] Krzeminska, D. M., Bogaard, T. A., Debieche, T. H., Cervi, F., Marc, V. and Malet, J. P., (2014). Field Investigation of Preferential Fissure Flow Paths with Hydrochemical Analysis of Small-Scale Sprinkling Experiments. *Earth Surface Dynamics*, Vol. 2(1); 181–195. https://doi.org/10.5194/esurf-2-181-2014.

[49] Travelletti, J., Sailhac, P., Malet, J. P., Grandjean, G. and Ponton, J., (2012). Hydrological Response of Weathered Clay–Shale Slopes: Water Infiltration Monitoring with Time-Lapse Electrical Resistivity Tomography. *Hydrological Processes*, Vol. 26(14); 2106–2119. https://doi.org/10.1002/hyp.7983.

[50] Gance, J., Malet, J.P., Supper, R., Sailhac, P., Ottowitz, D. and Jochum, B., (2016). Permanent Electrical Resistivity Measurements for Monitoring Water Circulation in Clayey Landslides. *Journal of Applied Geophysics*, Vol. 126; 98–115. https://doi.org/10.1016/j.jappgeo.2016.01.011.

[51] Huang, A. B., Lee, J. T. and Ho, Y. T., (2012). Stability Monitoring of Rainfall-Induced Deep Landslides through Pore Pressure Profile Measurements. *Soils and Foundations*, Vol. 52(4); 737–747. https://doi.org/10.1016/j.sandf.2012.07.013.

[52] Haugen, B. D., (2017). A Design Method for Landslide Surface Water Drainage Control. *Environmental & Engineering Geoscience*, Vol. 23(4); 275–289. https://doi.org/10.2113/gseegeosci.23.4.275.

[53] Sari, P. T. K., Mochtar, I. B. and Chaiyaput, S., (2023). Effectiveness of Horizontal Sub-Drain for Slope Stability on Crack Soil Using Numerical Model. *Geotechnical and Geological Engineering*, Vol. 41; 4821–4844. https://doi.org/10.1007/s10706-023-02550-1.